RSC Applied Polymers

ROYAL SOCIETY OF CHEMISTRY

PAPER

View Article Online
View Journal | View Issue

Cite this: *RSC Appl. Polym.*, 2024, **2**, 1170

A polyamide and polyethylene multilayer composite with enhanced barrier and mechanical properties at high temperature†

Weiqing Fang,[a] Yu Hui Cheng,[a] Adam Pearson,[a] Yige Huang,[a] Ashkan Dargahi,[a] Mark Duncan,[b] Joel Runka,[b] Ahmed Hammami[c] and Hani E. Naguib *[a]

An advanced multilayer thermoplastic composite, composed of Polyethylene of Raised Temperature (PERT), Polyamide 12 (PA12), and Maleic Anhydride Grafted Polyethylene (MA), has been developed for high-temperature, high-pressure applications. An adhesive layer consisting of 35–60–5 wt% PERT-PA12-MA (Blend), has been tailored to optimize adhesive strength between PERT and PA12 layers. The developed three-layer composite (Trilayer) demonstrated exceptional water vapor and CO_2 barrier properties by incorporating PERT as a water transmission retarder and PA12 as a CO_2 diffusion retarder. At 82 °C, the water vapor transmission rate and CO_2 permeability of Trilayer samples were 58%, and 31% lower than those of the Blend, respectively. The Trilayer samples exhibited an average Young's modulus that was 17% higher than that of the Blend, while the yield stress was similar to the Blend. In terms of creep resistance, the Trilayer samples showed a 29% and 40% reduction in tensile creep strain and creep rate, respectively, compared to the Blend. Additionally, the Trilayer samples achieved 48% and 39% decreases in flexural creep strain and creep rate, respectively, in the flexural creep test. The Trilayer also exhibited a 56% decrease in deformation under drop-weight impact and a 14% improved impact absorption compared to the Blend. The overall performance of the multi-layer thermoplastic composite made from PERT and PA12 constituents was significantly enhanced, aligning with the carbon footprint reduction initiative to substitute thermoset, metal, and other traditional materials.

Received 2nd July 2024,
Accepted 19th September 2024

DOI: 10.1039/d4lp00220b

rsc.li/rscapplpolym

1. Introduction

Addressing climate change stands as one of the current global key challenges. Developing a lower carbon footprint and more sustainable materials has become increasingly critical for all engineering sectors.[1–3] Traditional thermoset and metal materials are commercially used in the high service temperature pipeline and pressure vessel sectors. Reinforced thermoplastic composites facilitate a wide range of benefits including remelting capability, recyclability, lightweight construction, corrosion resistance, ease of processing, and low CO_2 emissions during production.[4] These attributes make them cleaner alternatives with lower carbon footprints than thermoset and metal materials.[4] They are being increasingly adopted in the pipeline, pressure vessel and other engineering sectors, driven by their significant environmental impacts and the stringent environmental regulations governing these industries.[5–7]

Polyethylene of Raised Temperature (PERT) is a recently developed thermoplastic that is widely used in pipelines and pressure vessels at elevated temperatures.[8] However, its inherent rubbery behaviour under high-temperature and high-pressure conditions renders it unsuitable for certain structural designs. This limitation stems from its restricted mechanical properties, lack of creep resistance, and insufficient gas barrier properties,[9] especially when exposed to hydrocarbons in general and aromatics in particular. Conversely, Polyamide 12 (PA12) exhibits a higher glass transition temperature (T_g) and glassier behaviour at high temperatures due to its restricted chain mobility from the hydrogen bonding interaction in its amide linkages.[10] PA12 is favored at elevated temperatures for its hydrocarbon resistance, thermal stability, stiffness, and creep resistance. However, the water absorption of PA12, and consequently its hydrolysis, negatively impacts its mechanical properties, modulus, fracture resistance, and impact resistance.[11]

[a]*Department of Mechanical and Industrial Engineering, University of Toronto, 5 Kings College Rd, Toronto, ON, M5S 3G8, Canada.*
E-mail: naguib@mie.utoronto.ca
[b]*Flexpipe, Mattr Corp., 3501 54th Ave. SE, Calgary, AB, T2C 0A9, Canada*
[c]*Flexpipe, Mattr Corp., 1103 Parsons Rd SW, Edmonton, AB, T6X 0X2, Canada*
† Electronic supplementary information (ESI) available. See DOI: https://doi.org/10.1039/d4lp00220b

Blending the polyamide and polyethylene thermoplastics, which have complementary properties, provides a feasible approach to developing a composite for large-scale, high-temperature and high-pressure applications,[12,13] while maintaining the environmental benefits of the thermoplastic materials.[14] The combination of PERT and PA12 addresses the challenge where the individual materials cannot meet all desired characteristics, including mechanical strength, impact resistance, stiffness, creep resistance, water resistance, gas barrier, and service temperature. Previous studies have primarily focused on mechanical reinforcement by leveraging the high tensile strength of PA12 while ignoring the advantages offered by PE.[15–17] J. Huitric *et al.* investigated the morphological and rheological behaviours of immiscible blends consisting of PE and PA12. The change in droplet size corresponding to different volume fractions resulted in alterations to the elasticity of the blends.[15] In the two similar studies conducted by Z. Denchev *et al.* and N. Dencheva *et al.*,[16,17] extruded microfibrillar composites were developed using oriented blends of PE and PA12 with enhanced strength due to the reinforcing fibrils of PA12. These studies focused on mechanical reinforcement, solely taking advantage of PA12.

Multilayer composites with flexible material selection and optimized hierarchical structure provide advanced solutions in large-scale manufacturing. In recent studies, a layering technique has been utilized to develop multilayer composites from dissimilar thermoplastics, achieving novel performances in energy absorption,[18,19] damping,[20] tunable shape memory behavior,[21] and flame retardation,[22,23] electromagnetic interference shielding.[24] This technique can extend to the development of a composite incorporating PERT and PA12. The layered structural design enables individual layers to contribute distinct properties, resulting in a multilayer composite with a unique combination of strength, damping, barrier properties, and other attributes. The development of multilayer composites using two or more dissimilar materials typically necessitates an adhesive layer to promote cohesive bonding among the heterogeneous layers. Thermoset adhesive materials are commercially available for development of multilayer composites. Due to the benefits of thermoplastic materials, recent interests have been raised in developing thermoplastic adhesive materials and thermoplastic multilayer composites.[25–28] C. Huang *et al.* used low-density polyethylene grafted with maleic anhydride (LDPE-*g*-MAH) as an adhesive layer to develop the three-layer composite film consisting of ethylene–vinyl alcohol copolymer (EVOH) and low-density polyethylene (LDPE).[25] High-density polyethylene grafted with maleic anhydride (HDPE-*g*-MAH) was also used as an adhesive layer to develop a layered composite with controlled barrier and tensile properties. However, these multilayer composites were limited to low temperature applications due to the relatively inferior mechanical properties of polyethylene-based adhesive, especially at elevated temperatures. C. Ge *et al.* developed a layered composite without an adhesive layer, relying instead on the adhesion between the selected thermoplastic materials and the fabrication method.[27] However, this approach cannot be generalized for the development of multilayer composites from thermoplastic materials characterized by low compatibility and adhesion properties, such as PE and PA12.[29] In a recent study, W. Fang *et al.* developed a carbon fiber-reinforced thermoplastic adhesive layer, which achieved improved high-temperature performance.[28]

This study aims to optimize the design of a three-layer composite by using a blend of PERT and PA12 as the adhesive layer, effectively bonding the PERT and PA12 layers without the need for an adhesive layer made of different materials. By utilizing just two thermoplastic primaries, this multilayered composite preserves the benefits of thermoplastics and presents a lower carbon footprint and economically viable solution compared to thermoset or metal counterparts. A T-peel test was used to evaluate the adhesion of the blend under controlled conditions. The overall performance of the multilayer thermoplastic composite was evaluated at the maximum operating temperature of PERT (82 °C)[30] to benchmark its performance. The barrier properties of the PERT/PA12 multilayer composite were characterized by water vapor transmission test and CO_2 permeability test, while the mechanical strength was assessed through the tensile test, creep test, and drop-weight impact test. The developed design method facilitates the feasibility of fine-tuning the ratio of composite materials to meet specific performance requirements in large-scale manufacturing while maintaining a compelling combination of safety, durability, CO_2 reduction, and sustainability. These latter attributes certainly align well with the global shift towards more sustainable technologies and yield invaluable assets across diverse sectors.

2. Experimental

2.1. Materials

PERT was supplied in pellet form with a density of 0.95 g cm^{-3}, a melting temperature of 132 °C and a melt flow rate of 0.1 g per 10 min at 190 °C per 2.16 kg. PA12 was also supplied in pellet form with a density of 1.02 g cm^{-3} and a melt temperature of 176 °C. Maleic anhydride grafted polyethylene (MA) in pellet form with a density of 0.95 g cm^{-3}, a melting temperature of 127 °C and a melt index of 5 g per 10 min (190 °C, 2.16 kg), and grafting level between 0.8% and 1.2% was used as the compatibilizer and adhesion promoter. The PA12 pellets were first dried in an oven at 60 °C for 48 h. As listed in

Table 1 Weight ratios of PERT-PA and PERT-PA-MA blends

PERT-PA blends		PERT-PA-MA blends		
PERT	PA12	PERT	PA12	MA
30%	70%	40%	60%	0%
40%	60%	37.5%	60%	2.5%
45%	55%	35%	60%	5%
50%	50%	30%	60%	10%
60%	40%			
70%	30%			

Table 1, PERT-PA12 and PERT-PA12-MA blend samples with different weight ratios were prepared by twin-screw compounding (DSM Xplore 15, DSM Netherlands) at 230 °C, with a residence time of 10 min, and a screw speed of 200 rpm. PA12, PERT, and blend samples were compression molded into bar and film samples at 230 °C. The process involved melting the pellets for 5 min, hot pressing them under 5 tons of hydraulic pressure for an additional 5 min, and then allowing them to air cool. Three individual layers, each with a thickness of 0.34 mm, were stacked in the order of PA12, blend, and PERT. Then, the stacked layers were compression molded to 1 mm thick Trilayer samples in a vacuum bag at 230 °C for 5 min and then air-cooled. The schematic of fabrication method was illustrated in ESI.† The thickness of the PA12, PERT, blend, and Trilayer samples were 1.01 ± 0.055 mm, 0.98 ± 0.035 mm, 1.04 ± 0.028 mm, and 1.04 ± 0.062 mm, respectively. In the layered structure, the blend served as the adhesive layer, and its adhesion strengths to both PA12 and PERT layers were characterized to compare the performance of different blends and determine the optimized weight ratio.

2.2. Measurement of adhesion strength at elevated temperatures

Adhesion strength measurement at elevated temperature was conducted using the previously developed T-peel test method.[28] T-peel tests were performed under isothermal temperatures of 30 °C and 82 °C, respectively, using a Dynamic Mechanical Analyzer (DMA, MCR 702e MultiDrive, Anton Paar). The specimens were equilibrated for 5 min at the desired testing temperature. Subsequently, T-peel testing was conducted at a constant adhesive separation rate of 250 μm min^{-1} in a range of 0 to 7500 μm. The force was recorded and plotted against peeled distance. The peel strength of the adhesive layer was calculated as the average force per width of the specimen after the initial load peak. At least 3 replicates were conducted, and the standard deviations were used as the error bar. Same method was applied to the other characterizations to ensure the consistency.

2.3. Morphological and crystallinity study of the blend system

PERT-PA and PERT-PA-MA blends were cryosectioned by an ultramicrotome (Leica Ultracut UTC) for scanning electron microscopy (SEM, JSM-IT100, JEOL). An industrial-grade diamond knife was used to cut the sample at −120 °C, which was below the T_g of PERT, PA12, and MA. The cryosectioned surfaces were sputter-coated with a thin gold layer measuring 15 nm in thickness prior to imaging.[31] Differential Scanning Calorimetry (DSC Q2000, TA Instruments) tests were conducted by heat–cool–heat cycling process between 30 °C and 200 °C with heating and cooling rates of 10 °C min^{-1} under a nitrogen atmosphere. The measured heat flow in the second heating phase was used to determine the melting temperature (T_m), and degree of crystallinity.

2.4. Characterization of barrier properties

The water vapor barrier properties of PA12, PERT, Blend and Trilayer samples at an elevated temperature were characterized by water vapor transmission testing following ASTM E96.[32] Thin film test specimens with a thickness of 1 mm were installed into permeability cups (VF2201-111, TQC). The permeability cups, containing deionized water, have a 25 cm^2 permeation area for the transmission of water vapor through the film specimens. The cups were placed inside an oven at an elevated temperature of 82 °C. Daily weight measurements of the permeability cups were taken to determine the average weight loss until reaching a steady state. The water vapor transmission rate was calculated using the daily steady state weight loss in terms of mg cm^{-2} day^{-1}.

The CO_2 barrier properties of PA12, PERT, Blend, and Trilayer samples were measured using a permeation cell developed in a previous study by Dargahi *et al.*[33,34] Discs of 7.6 mm in diameter with 1 mm thickness were cut from the compression molded films for the permeation tests. The permeation tests were conducted under 1500 psi feed pressure CO_2 at 82 °C. The coefficients of permeability (Pe), diffusivity (D), and solubility (S) were identified using the time lag method as described in the previous study.[33]

2.5. Tensile and Young's modulus

A DMA (MCR 702e MultiDrive, Anton Paar), using a solid rectangular fixture for a linear drive, was used to characterize the yield stress and elastic modulus of PA12, PERT, Blend and Trilayer samples. The 3.5 mm by 15 mm test specimens were cut from compression molded 1 mm thick film. During the test, the specimens were equilibrated at 82 °C for 5 minutes. Subsequently, the specimens were extended linearly to a strain of 250% at a rate of 20% per minute, with stress and strain measured simultaneously. The yield stresses for PA12, PERT, blend, and Trilayer samples were calculated using a 1% offset strain based on ASTM D638. Young's modulus was determined from the slope of stress–strain curve between 0.5% and 1.5% strain.

2.6. Tensile and flexural creep resistance

The resistance of PA12, PERT, Blend and Trilayer samples to both tensile and flexural creep was characterized using a DMA (MCR 702e MultiDrive, Anton Paar) following the test method in previous tensile creep study[35] and flexural creep study,[36] respectively. The 3.5 mm by 15 mm by 1 mm test specimens were equilibrated at 82 °C for 5 min, followed by applying a constant 2 MPa tensile load for 30 min, which was below the yield stress of all the materials. The creep resistance was characterized using the total tensile strain at 30 min, as well as the average creep strain rate in the last 5 min of the test. Flexural creep test specimens, with the same dimensions as the tensile creep specimens, were mounted into a cantilever clamp. In single cantilever bending, one end of the specimens was mounted into a fixed clamp with the other end in the moveable clamp. After equilibration at 82 °C for 5 min, a constant 20 MPa bending stress was applied to the specimen for

30 min. The flexural strain was calculated as the ratio of the deformation at the loading end over the beam length. Similar to tensile creep resistance, the flexural creep resistance was characterized using the flexural strain at 30 min, as well as the average creep strain rate in the final 5 min.

2.7. Impact absorption

Drop-weight impact tests in accordance with ASTM D7766, were conducted to characterize the impact absorption of PA12, PERT, blend and Trilayer samples. A 230 g cylindrical striker with ball head was released from a 1 m height, following the same procedures in previous studies.[37,38] Disc specimens with a 2.46 cm diameter were cut from the 1 mm thick film and placed under the striker. Trilayer specimens were oriented with the PA12 layer coming into first contact with the striker. The force transmitted into the materials was recorded by a load cell beneath the specimens. The impact location of the specimens was sectioned to quantify the deformation.

3. Results and discussion

3.1. Optimization of adhesive layer in PA12/Blend/PERT multilayer composite

Multilayer composites, with two or more dissimilar polymer layers, necessitate an adhesive layer to bond the dissimilar layers.[26–28] The adhesion strength of such adhesive layers determines the ability to sufficiently bond constituent layers,[28] being PA12 and PERT in this study. In the design of the multilayer composite, as illustrated in Fig. 1(a), the blends have the potential to bond both PA12 and PERT layers. Initially in the study, design optimization was employed to improve the adhesive strength of the blends at both 30 °C and 82 °C. One of the key considerations was to balance the adhesion strength to both PERT and PA12 to ensure effective load transfer in the multilayer composite and prevent delamination at the more vulnerable interface. A T-peel test setup was employed to characterize the adhesion strength of the blend system, as

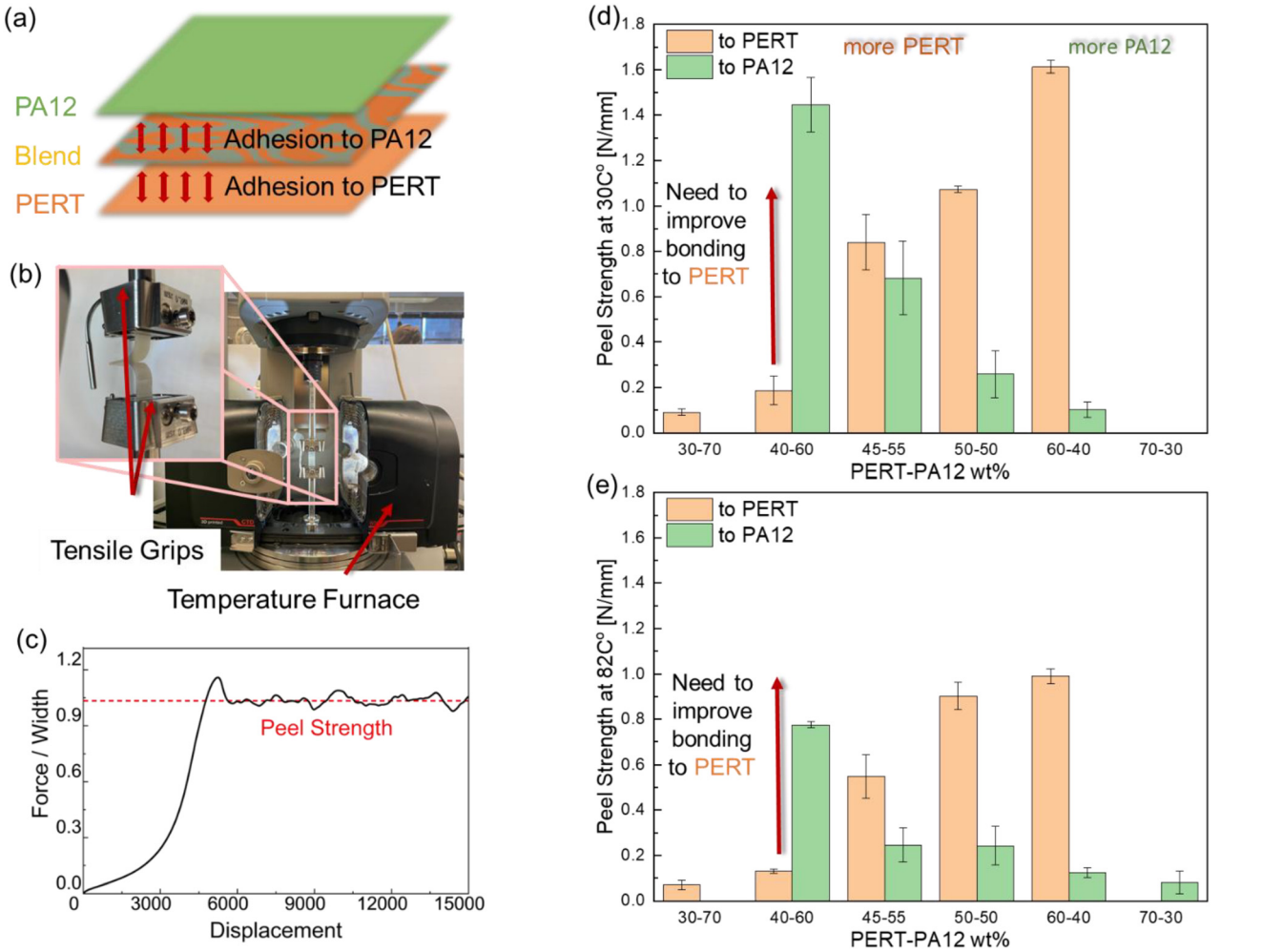

Fig. 1 T-peel test setup and measured peel strength of PERT-PA12 blends to PERT and PA12. (a) Schematic of Trilayer sample, which uses an immiscible blend as an adhesion layer to bond the two dissimilar layers. (b) T-peel test setup consisting of tensile grips and temperature furnace. (c) Example of force/width *vs.* displacement curve and peel strength at the steady-state plateau. Peel strength of PERT-PA12 to PERT and PA12 at (d) 30 °C, and (e) 82 °C.

shown in Fig. 1(b). As the example illustrates in Fig. 1(c), the peel strength was calculated as the average value of the plateau region in the force/width *vs.* displacement curve. The peel strengths of PERT-PA12 blends to both PERT and PA12 substrates at 30 and 82 °C are shown in Fig. 1(d) and (e), respectively. At both temperatures, the peel strengths of the PERT-PA12 blends to PERT increased as the weight percentage of PERT was raised. Meanwhile, higher peel strengths to PA12 were obtained with a higher weight percentage of PA12 in the blends. The 40%–60% PERT-PA12 blend system demonstrated imbalanced adhesion strength to PERT and PA12. An improved adhesion strength to PERT is required to prevent the delamination in PA12/blend/PERT Trilayer composite.

A promising approach is to use MA as the compatibilizer and adhesion promoter through hydrogen bonding, polar–polar interactions, or covalent bonding between the polyolefin and the polar surface.[39–42] Additions of MA were thus incorporated into the preparation of three PERT-PA12-MA blends with composition targets of 37.5–60–2.5, 35–60–5, and 30–60–10 wt%, respectively. The morphology of the blends without and with MA compatibilizer are shown in Fig. 2(a) and (b), respectively. An immiscible morphology was observed in both non-compatibilized and compatibilized blends. PA12 exists as dispersed droplets within the continuous phase of PERT. MA addition resulted in a significantly smaller and better dispersed PA12 phase. The crystallinities of PA12, PERT, and 35–60–5 PERT-PA12-MA blend samples were characterized using DSC, as shown in Fig. 2(c) and summarized in Fig. 2(d). The heat flow curves display single peaks for both PA12 and PERT, with the blend samples exhibiting the same single peaks, indicating no evidence of eutectic mixture.[43]

In the T-peel test, the adhesion strengths to PERT increased with the addition of 2.5 and 5 wt% MA at both testing temperatures compared to the blend without MA, as shown in Fig. 2(e) and (f). With 5 wt% MA, the adhesion strength was significantly improved by 199% and 309% at 30 °C and 82 °C, respectively. However, with a further increase of MA to 10 wt%, the adhesion strength to PERT was unchanged at 30 °C and decreased at 82 °C. This was likely due to the low mechanical strength of MA which resulted in cohesive failure of the Blend at elevated temperature. The most balanced adhesion strength to both the PERT and PA12 was obtained in the case of the 35–60–5 PERT-PA12-MA blend. This blend (Blend) was selected for further characterization and for the design of the three-layer composite (Trilayer). Thermogravimetric analysis was used to demonstrate the stability of Trilayer composites in ESI.†

3.2. Enhanced barrier properties of the multilayer composite

The barrier properties of PA12, PERT, Blend, and Trilayer were characterized by water vapor and supercritical CO_2 permeation tests at 82 °C. The orientation of the Trilayer samples for water vapor and CO_2 diffusion was determined based on the different barrier properties of PERT and PA12, illustrated in Fig. 3(a).

3.2.1. Water vapor barrier properties. In the water vapor test, the water vapor transmission rate of PA12 was measured as 2.19 mg cm^2 day^{-1}, which was 742.3% higher than that of PERT, 0.26 mg cm^2 day^{-1}. This is due to a high affinity for forming an intermolecular hydrogen bond between the amide groups and water, which attracts water vapor from the environment.[44] In contrast, PERT along with similar polyethylene-based materials, are known for their resistance to water vapor transmission and are commonly used as water vapor barrier layers. The water vapor transmission rate of the Blend was measured as 0.80 mg cm^2 day^{-1}, which is 207.7% higher than PERT and 63.5% less than PA12. The reduction compared to PA12 is based on the 40% polyethylene content in the Blend. The PERT is a continuous phase providing an improved barrier effect stemming from limited percolation of the PERT phase.[45–47]

For the water vapor test of Trilayer samples, the test specimens were orientated such that the PERT layer was exposed first to the water vapor, taking advantage of its superior water vapor resistance. The water vapor transmission rate of Trilayer samples was measured as 0.34 mg cm^2 day^{-1} at 82 °C, which is 30.8% higher than that of PERT, 84.5% less than PA12, 57.5% less than the Blend, and 37.5% less than the estimated value using the series model for the transmission rate:[48]

$$\mathrm{TR} = \frac{1}{\Phi_a/\mathrm{TR}_a + \Phi_b/TR_b + \Phi_c/\mathrm{TR}_c \ldots} \quad (1)$$

where, TR_a, TR_b, TR_c, and Φ_a, Φ_b, Φ_c are the transmission rate and volume fraction of the constituent layers. The water vapor transmission rate of the Trilayer is low considering the overall PERT content in Trilayer is similar to the Blend. In this anisotropic structure, the PERT layer acts as a water vapor retarder which significantly reduces the ingress of water vapor into the Blend and PA12 layers. High water barrier property of PERT reduced the intermolecular hydrogen bond in PA12 layer. Thus, the layered structure incorporating PERT as a retarder demonstrated notable water vapor barrier property. Furthermore, thermogravimetric analysis and tensile tests were conducted on the Trilayer specimens before and after WVT tests to demonstrate the stability in high-temperature water vapor environment, as shown in ESI.†

3.2.2. CO_2 barrier properties. The CO_2 gas barrier properties were characterized using the 82 °C and 1500 psi supercritical CO_2 permeation test. The time-lag method was used to calculate the diffusivity, solubility, and permeability of the material,[33] as illustrated in Fig. 3(c). The diffusivity and permeability values were determined using the *x*-intercept and slope of the downstream pressure curve at steady-state. The time-lag method yields accurate results for permeation but may introduce uncertainties of approximately 10–15% when predicting diffusivity due to errors associated with the transition state.[49] Due to the substantial difference in constituent material properties, the time-lag method is still applicable for

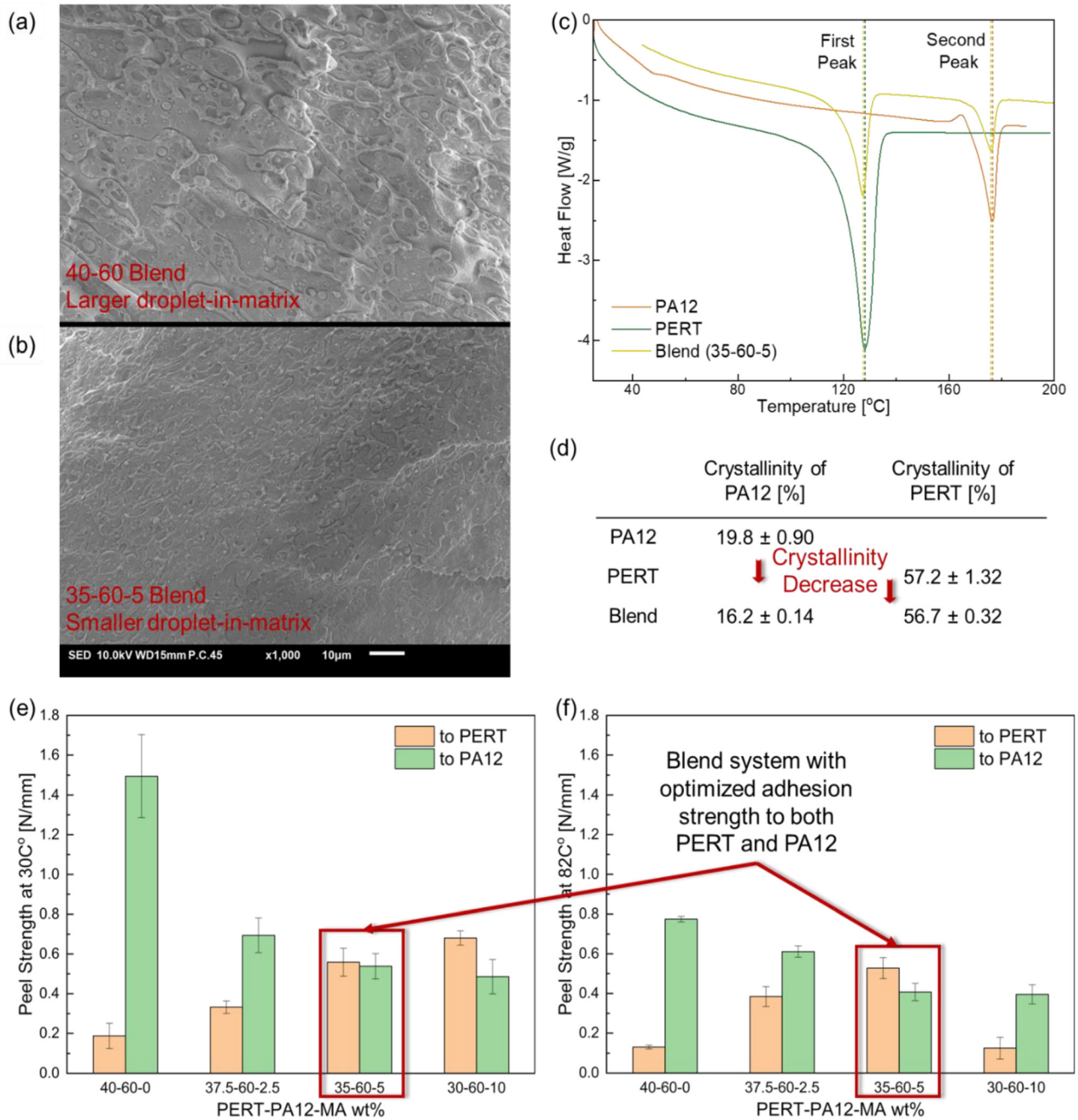

Fig. 2 Morphology, crystallinity, and adhesion strength of PERT-PA12-MA blends. SEM images of (a) PERT-PA12 40–60 blend and (b) PERT-PA12-MA 35–60–5 blend. Smaller immiscible phases were observed with MA as compatibilizer. (c) Heat flow *vs.* temperature curves of PA12, PERT, and Blend (35–60–5). First and second peaks in Blend are consistent to the intrinsic peaks. No addition peak was observed, confirming no copolymerization between two dissimilar materials. (d) Calculated crystallinity of PA12, PERT and Blend. Crystallinities of Blend were lower than the intrinsic materials. Peel strength of PERT-PA12-MA at (e) 30 °C, and (f) 82 °C.

the qualitative comparison between PA12, PERT, Blend, and Trilayer.

Gas diffusivity depends on the length and tortuosity of the diffusion path between the crystal spherulites. As shown in both Fig. 3(d) and (e), the diffusivity of PA12, measured at 0.837×10^{-6} cm^2 s^{-1}, is 71.9% lower than the 2.977×10^{-6} cm^2 s^{-1} of PERT. PA12 has a much higher T_g and has constrained chain mobility due to the hydrogen bonding in its amide linkages.[10] Thus, the restricted chain segmental mobility in the amorphous phase of PA12 yields a significantly lower CO_2 gas diffusivity. Solubility is another term contributing to CO_2 permeability. The calculated CO_2 solubility of PA12 was 1.484 cm^3

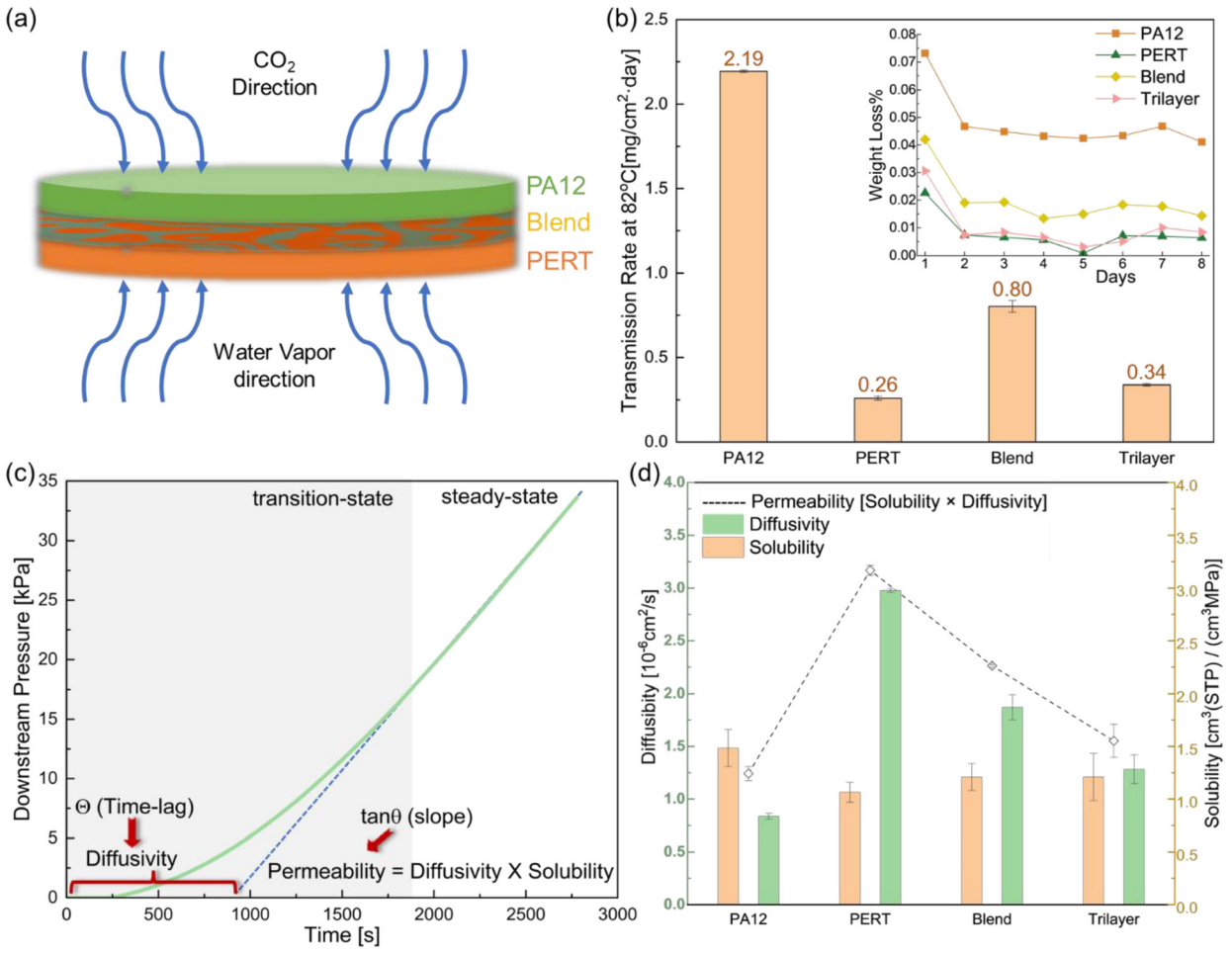

(e)

	Water Vapor Transmission Rate [$mg/cm^2 day$]	Diffusivity [$10^{-6} cm^2/s$]	Solubility [$\frac{cm^3(STP)}{cm^3 MPa}$]	Permeability [$10^{-6} \frac{cm^3(STP)}{cm \cdot s \cdot MPa}$]
PA12	2.19	0.837	1.484	1.242
PERT	0.26	2.977	1.065	3.169
Blend	0.80	1.872	1.209	2.263
Trilayer	0.34	1.283	1.210	1.553

Fig. 3 Barrier properties, *i.e.*, water vapor and CO_2 permeability, of PA12, PERT, Blend and Trilayer. (a) Schematics of permeation test on water vapor and CO_2 with different transmission directions. (b) Measured weight loss % of water vapor and calculated transmission rate at 82 °C. Trilayer sample showed comparable water vapor barrier property to PERT. (c) Example of downstream pressure *vs.* time curve from CO_2 permeation test at 82 °C, and extracted CO_2 permeability from slope, and CO_2 diffusivity from *x*-intercept. (d) and (e) Calculated CO_2 diffusivity, solubility, and permeability of PA12, PERT, Blend, and Trilayer at 82 °C. Trilayer sample showed comparable CO_2 barrier property to PA12.

(STP) (cm^3 MPa)$^{-1}$ which was 39.3% greater than PERT. PA12 exhibits a more asymmetrical molecular structure, leading to higher polarity and cohesive energy density.[50] Consequently, PA12 demonstrates more interaction with CO_2 and higher solubility. The permeabilities of PA12 and PERT were measured as 1.242×10^{-6} cm^3 (STP) (cm s MPa)$^{-1}$ and 3.169×10^{-6} cm^3 (STP) (cm s MPa)$^{-1}$, respectively. PERT and PA12 display distinct CO_2 permeability characteristics. More specifically, PERT has a higher diffusivity term due to its crystal spherulites, while PA12 has a higher solubility term due to its polarity.

The diffusivity and solubility of the Blend were 1.872×10^{-6} cm^2 s^{-1} and 1.209 cm^3 (STP) (cm^3 MPa)$^{-1}$, respectively. As shown in Fig. 2(b), PERT phase wrapped PA12 phase in the droplet-in-matrix morphology of the Blend, reducing the interaction between CO_2 and PA12. Consequently, the solubility of the Blend was lower than PA12, and slightly higher than PERT. Meanwhile, the additional diffusion paths in the interface between immiscible phases contribute positively to the high diffusivity of the Blend. A permeability of 2.263×10^{-6} cm^3 (STP) (cm s MPa)$^{-1}$ was obtained for the Blend, 28.6% lower

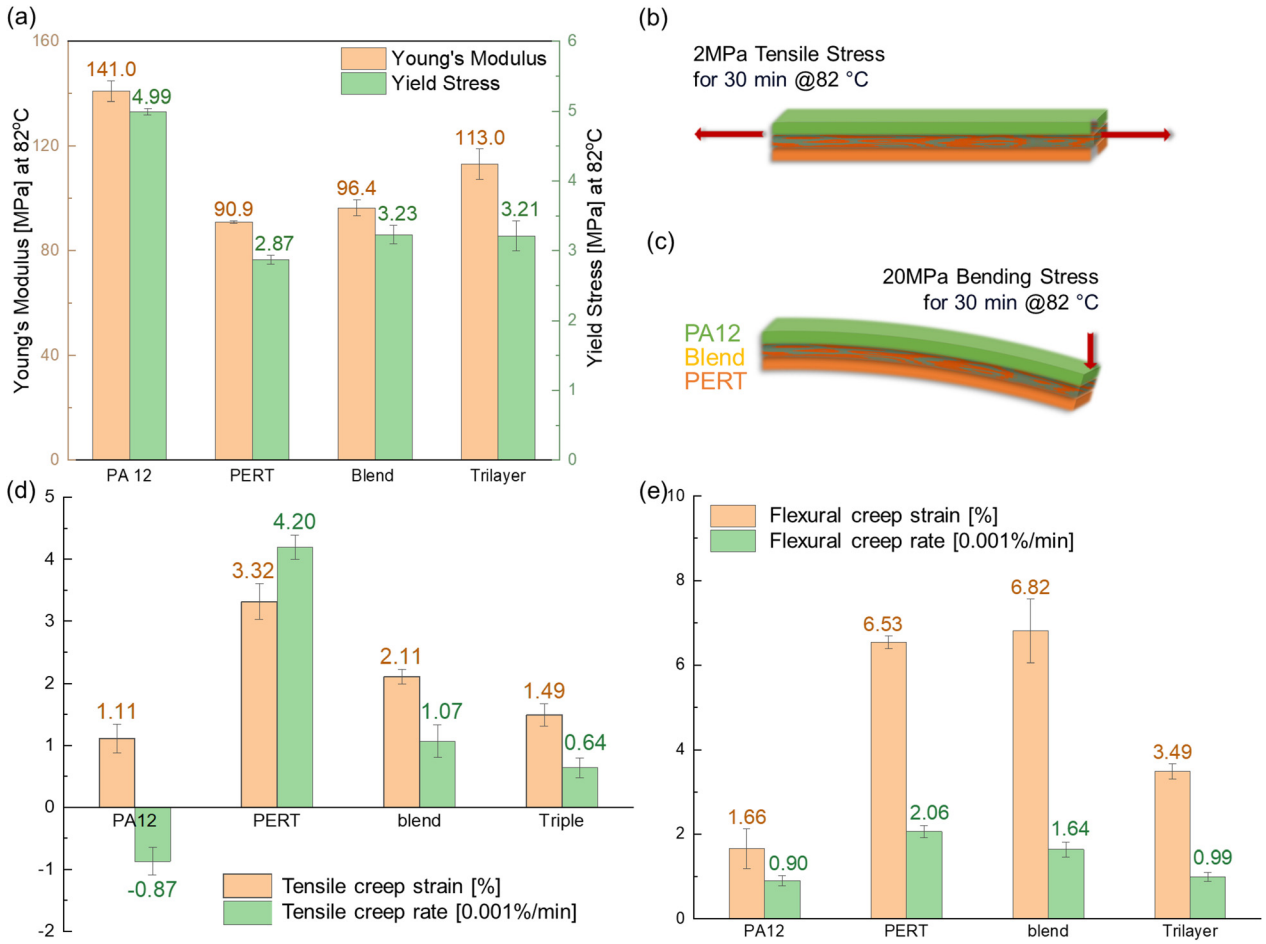

Fig. 4 Dynamic mechanical properties: tensile properties, creep, and flexural creep resistance of PA12, PERT, Blend and Trilayer. (a) Measured Young's modulus and yield stress results in tensile test at 82 °C. Schematics of (b) tensile and (c) flexural creep tests under tensile stress and bending stress, respectively, at 82 °C for 30 min. Measured strain, and creep rate at 82 °C in (d) tensile creep and (e) flexural creep test. Trilayer shows comparable creep and flexural creep resistances to PA12, and significantly better than Blend.

than PERT, 82.2% higher than PA12, and 18.4% higher than the estimated value of 1.911×10^{-6} cm^3 (STP) (cm s MPa)$^{-1}$ using the Maxwell's model for the droplet-in-matrix morphology:[47]

$$P = P_m\left[\frac{P_d + 2P_m - 2\Phi_d(P_m - P_d)}{P_d + 2P_m + \Phi_d(P_m - P_d)}\right] \quad (2)$$

where, P_d, and P_m are the permeabilities of the droplet phase, and matrix phase, respectively. Φ_d is the volume fraction of the droplet phase. The Blend shows reduced solubility yet increased diffusivity. These opposing effects lead to a marginal improvement in CO_2 barrier properties.

The Trilayer samples were orientated with the PA12 layer exposed to pressurized CO_2 to leverage its lower CO_2 diffusivity. The diffusivity, solubility, and permeability of Trilayer were determined as 1.283×10^{-6} cm^2 s^{-1}, 1.210 cm^3 (STP) (cm^3 MPa)$^{-1}$, and 1.553×10^{-6} cm^3 (STP) (cm s MPa)$^{-1}$, respectively. The measured permeability of Trilayer was 51.0% lower than PERT, 25.0% higher than PA12, 31.4% lower than Blend, and 19.1% lower than the estimated value of 1.920×10^{-6} cm^3 (STP) (cm s MPa)$^{-1}$ using the series model for permeation:[47]

$$P = \frac{L}{L_a/P_a + L_b/P_b + L_c/P_c \ldots} \quad (3)$$

where, P_a, P_b, P_c, and *etc*. are the permeabilities of constituent layers. L_a, L_b, L_c, and *etc*. are the thicknesses of constituent layers. The PA12 layer in the multilayer structure acted as diffusion retarder, reducing the CO_2 diffusion through the Blend and PERT layers. Overall, the CO_2 Trilayer barrier properties were marginally lower than PA12, and significantly better than PERT and Blend.

3.3. Enhanced mechanical properties of the multilayer composite

3.3.1. Tensile modulus and yield stress. Fig. 4(a) shows Young's modulus and yield stress of PA12, PERT, Blend and Trilayer samples. The Trilayer yielded a higher Young's modulus and yield stress than the Blend, positioned between the corresponding values of PA12 and PERT. Young's modulus

and yield stress of the Blend were 96.4 MPa and 3.23 MPa, respectively, demonstrating insignificant improvement over PERT. In the droplet-matrix immiscible morphology, phase separation results in inferior mechanical properties due to poor adhesion and impaired stress transfer between the PERT and PA12 phases.[51] The Young's modulus of the Trilayer exceeded that of the Blend samples by 17.2%, while the yield stress was comparable. The modulus of the Trilayer was calculated as 113.0 MPa which closely aligned with the estimated value of 109.4 MPa obtained using the rule of mixtures. The observed low yield stress in Trilayer samples is primarily attributed to the inherent low yield stress of the PERT and Blend layers. These layers yield prematurely in comparison to the PA12 layer, leading the Trilayer composite to exhibit yield stress comparable to the PERT and Blend, and lower than the PA12.

3.3.2. Tensile and flexural creep resistance. The creep tests were conducted under tensile and bending stress at 82 °C, as illustrated in Fig. 4(b) and (c), respectively. The tensile strain at 30 min and the average creep strain rate recorded from 25 min to 30 min are illustrated in Fig. 4(d). In the tensile creep test, 2 MPa tensile stress was applied to PA12, PERT, Blend and Trilayer samples. In the tensile creep test, the Trilayer demonstrated lower creep strain and creep rate value than the Blend, by 29.4% and 40.2%, respectively. The flexural creep strains and creep rates of PA12, PERT, Blend, and Trilayer under 20 MPa bending stress at 82 °C for 30 min are illustrated in Fig. 4(e). The Blend samples exhibited the highest 30 min flexural creep strain of 6.82% and an intermediate flexural creep rate of 0.00164% min^{-1}. The Trilayer exhibited a lower flexural creep strain and a lower flexural creep rate than the Blend by 48.8% and 39.6%, respectively. In both tensile and flexural

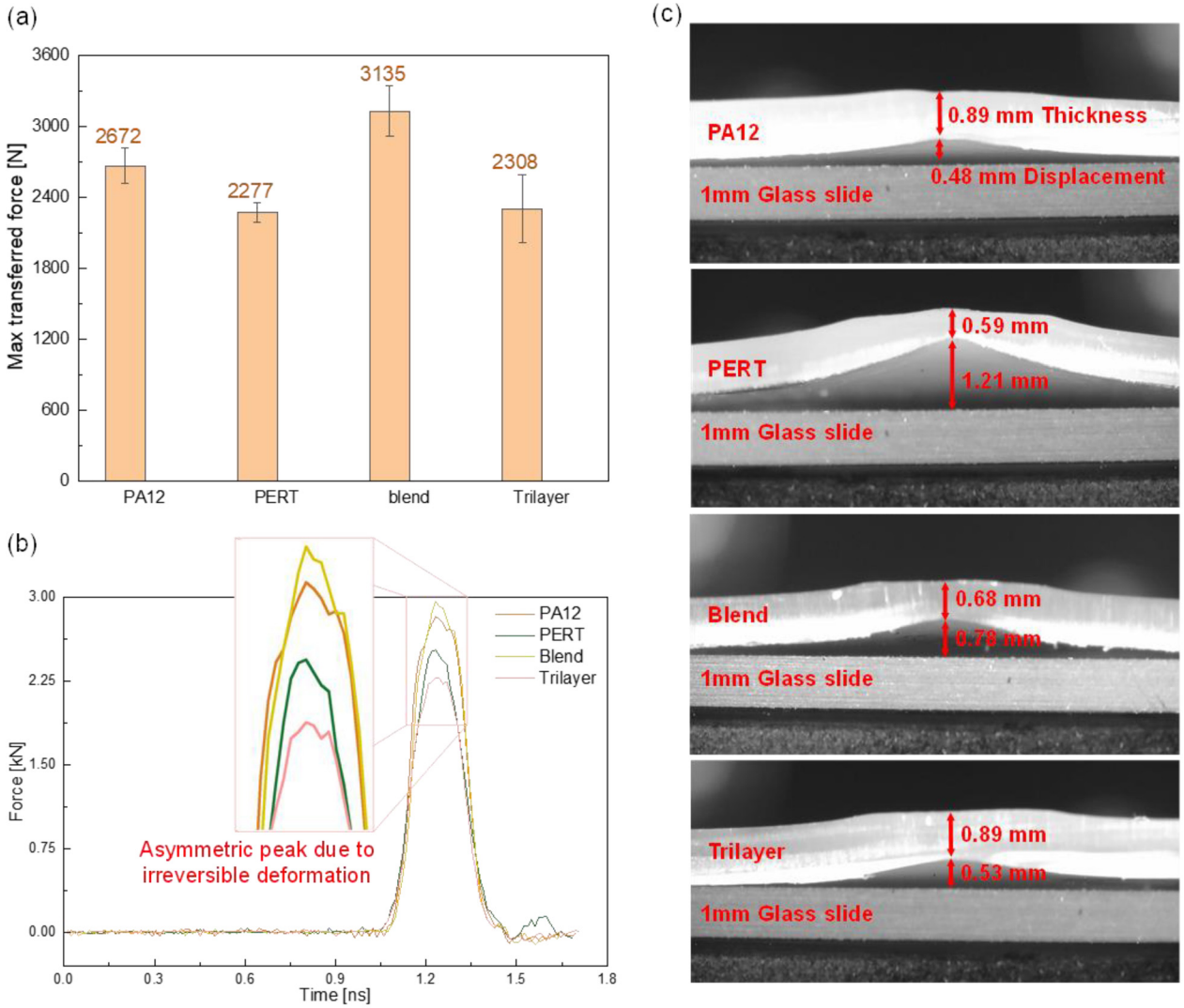

Fig. 5 Ball drop impact test of PA12, PERT, Blend and Trilayer. (a) Obtained max transferred force of PA12, PERT, Blend and Trilayer, showing Trilayer structure has optimized impact absorption than Blend. (b) Sample force *vs.* time curves from the ball drop impact test, showing the asymmetric peak resulting from partially reversible deformation of samples. (c) Sample images of PA12, PERT, Blend and Trilayer, indicating the thickness and deformation at the center of the impact.

creep tests, the Trilayer showed improved creep resistance over the Blend.

Compared to PERT, PA12 has much higher creep resistance at 82 °C in both tensile and bending creep tests, benefiting from its restricted chain segmental mobility and the resultant stiffness at an elevated temperature. A negative creep rate of PA12 was obtained in the tensile creep test due to the time-dependent volume contraction in its amorphous region when exposed to a temperature exceeding the T_g.[52,53] The Blend samples displayed moderate tensile and poor flexural creep resistance, attributed to the deformation occurring at the interface of the immiscible PERT and PA12 phases. The positive Gibbs free energy of the system causes the polymers to be thermodynamically immiscible, weakening the interfacial adhesion.[54] The interfaces between the distinct phases serve as the area of concentrated deformation when subjected to the bending stress, leading to significantly low creep resistance.[55]

In Trilayer samples, the strain was the same across the layers, which behaved like a parallel string system under tensile load. The PA12 layer, being stiffer, sustained more of the tensile stress, whereas the Blend and PERT layers sustained less. This configuration allowed the PA12 layer to bear more loading in the tensile creep test, leading to a creep performance similar to that of PA12. In the flexural creep test using the cantilever bending setup, tensile stress was present above the neutral axis, while compressive stress occurred below it. In the Trilayer samples, the PERT layer sustained compression, and the PA12 layer was subjected to tension. The layered structure leveraged the constituent layer, PA12, and exhibited an improved flexural creep resistance. Significantly improved creep resistance of the Trilayer was demonstrated compared to PERT and the Blend in both tensile and flexural creep tests.

3.3.3. Impact absorption and resistant to deformation. For the impact test at ambient temperature, the same drop-weight loading was applied to PA12, PERT, Blend and Trilayer samples. The impact absorption of the samples was compared based on the maximum transferred force from drop-weight load,[37,38] as illustrated in Fig. 5(a). The Blend achieved the highest maximum transferred force. This is attributed to the inability to absorb and propagate energy between the immiscible PERT and PA12 phases. PA12 also exhibited high maximum transferred force, owing to its glassy properties at the test temperature. PERT exhibited the lowest maximum transferred force, due to the rubbery behaviour and damping characteristics. Using a PERT layer as the impact absorber, the Trilayer effectively absorbed the drop-weight loading with a maximum transferred force comparable to PERT and 14% lower than Blend. The impact force *vs.* time plot in Fig. 5(b), showing the impact force transferred through each type of sample during the drop-weight impact test. The impact force experienced a sharp peak corresponding to engagement, stop, and rebound of the impactor as described by Belingardi and Vadori.[56] The kinetic energy transfers into the test specimen until the maximum transferred force is reached. While the energy is being absorbed by the specimens for all samples, the asymmetry of the peaks was due to the impact energy exceeding their elastic limits, causing irreversible and permanent deformation of the samples.

Deformation of the tested samples is illustrated in Fig. 5(c). All samples exhibit noticeable deformation from the same level of impact. PA12 and the Trilayer exhibited less deformation than PERT and the Blend. PA12 had the lowest permanent deformation and superior resistance to the drop-weight impact, attributed to its higher modulus and glassy behaviour at the testing temperature. PERT demonstrated the lowest resistance to the same impact, due to its lower modulus and rubbery behaviour. For the Trilayer, the PA12 layer was strategically placed to withstand the impact and thereby protect the Blend and PERT layers beneath. This configuration allowed the Trilayer to attain comparable deformation to PA12 and 56% less deformation than the Blend. Overall, the layered structural configuration excelled in both impact absorption and resistance to deformation, comparable to PERT and PA12, respectively.

4. Conclusions

In this study, a multilayer thermoplastic composite was developed, comprising of PA12 and PERT as outer layers, and a 35–60–5 wt% PERT-PA12-MA blend as an adhesive layer. Compared to the PERT-PA12-MA blend, the Trilayer demonstrated a reasonably low rate of water vapor transmission rate at 82 °C by incorporating PERT as a water vapor retarder. CO_2 barrier performance was enhanced by employing PA12 as a diffusion barrier and leveraging the low solubility of the Blend and PERT layers. During tensile testing at 82 °C, the Trilayer samples showed enhanced Young's modulus and yield stress compared to the Blend and PERT. Furthermore, the Trilayer leveraged the PA12 layer as the structural component to withstand continuous tensile and flexural stress, demonstrating superior creep resistance. By incorporating a PA12 layer to withstand direct impact and a PERT layer to dampen the impact energy, the Trilayer samples exhibited improved impact absorption and resistant to deformation from impact. This study developed a multilayer thermoplastic composite that features improved barrier and mechanical properties, aligning with CO_2 reduction efforts and offering an alternative to traditional materials such as thermoset and metal. The study presented an innovative approach to developing advanced thermoplastic composites, promoting a more sustainable and environmentally friendly future for thermoplastic materials.

Data availability

The data for this article cannot be shared due to confidentiality reasons.

Conflicts of interest

The authors declare that they have no conflict of interest.

Acknowledgements

The authors would like to greatly acknowledge the financial support of the Natural Sciences and Engineering Research Council of Canada (NSERC) and Mattr Infratech.

References

1 S. B. Abd Karim, S. Norman, S. Koting, K. Simarani, S. C. Loo, F. A. Mohd Rahim, *et al.*, Plastic Roads in Asia: Current Implementations and Should It Be Considered?, *Materials*, 2023, **16**(16), 5515.
2 J. Chen, L. Zhang, L. Wang, M. Kuang, S. Wang and J. Yang, Toward carbon neutrality: Selective conversion of waste plastics into value-added chemicals, *Matter*, 2023, **6**(10), 3322–3347.
3 A. K. Maurya, F. M. de Souza, T. Dawsey and R. K. Gupta, Biodegradable polymers and composites: Recent development and challenges, *Polym. Compos.*, 2024, **45**(4), 2896–2918.
4 R. A. Witik, J. Payet, V. Michaud, C. Ludwig and J. A. E. Månson, Assessing the life cycle costs and environmental performance of lightweight materials in automobile applications, *Composites, Part A*, 2011, **42**(11), 1694–1709.
5 Y. B. Shim, I. Y. Lee and Y. B. Park, Predicting the material behavior of recycled composites: Experimental analysis and deep learning hybrid approach, *Compos. Sci. Technol.*, 2024, **249**, 110464.
6 P. Jagadeesh, S. Mavinkere Rangappa, S. Siengchin, M. Puttegowda, S. M. K. Thiagamani, M. Hemath Kumar, *et al.*, Sustainable recycling technologies for thermoplastic polymers and their composites: A review of the state of the art, *Polym. Compos.*, 2022, **43**(9), 5831–5862.
7 H. Mohit, S. Mavinkere Rangappa, S. Siengchin, S. Gorbatyuk, P. Manimaran, C. Alka Kumari, *et al.*, A comprehensive review on performance and machinability of plant fiber polymer composites, *Polym. Compos.*, 2022, **43**(1), 608–623.
8 D. Schramm, PE-RT: A New Class of Polyethylene for Industrial Pipes, in *Safety and Reliability; Materials Technology; Douglas Faulkner Symposium on Reliability and Ultimate Strength of Marine Structures*, ASMEDC, 2006, vol. 3, pp. 513–521.
9 J. P. Greene, Microstructures of Polymers, in *Automotive Plastics and Composites*, Elsevier, 2021, pp. 27–37.
10 N. Ma, W. Liu, L. Ma, S. He, H. Liu, Z. Zhang, *et al.*, Crystal transition and thermal behavior of Nylon 12, *e-Polymers*, 2020, **20**(1), 346–352.
11 G. Baschek, G. Hartwig and F. Zahradnik, Effect of water absorption in polymers at low and high temperatures, *Polymer*, 1999, **40**(12), 3433–3441.
12 N. Vidakis, M. Petousis, L. Tzounis, A. Maniadi, E. Velidakis, N. Mountakis, *et al.*, Sustainable Additive Manufacturing: Mechanical Response of Polyamide 12 over Multiple Recycling Processes, *Materials*, 2021, **14**(2), 466.
13 M. Häußler, M. Eck, D. Rothauer and S. Mecking, Closed-loop recycling of polyethylene-like materials, *Nature*, 2021, **590**(7846), 423–427.
14 D. D. P. Moreno and C. Saron, Influence of compatibilizer on the properties of low-density polyethylene/polyamide 6 blends obtained by mechanical recycling of multilayer film waste, *Waste Manage. Res.*, 2018, **36**(8), 729–736.
15 J. Huitric, P. Médéric, M. Moan and J. Jarrin, Influence of composition and morphology on rheological properties of polyethylene/polyamide blends, *Polymer*, 1998, **39**(20), 4849–4856.
16 Z. Denchev, M. J. Oliveira and O. S. Carneiro, Nanostructured Composites Based on Polyethylene–Polyamide Blends. I. Preparation and Mechanical Behavior, *J. Macromol. Sci., Part B: Phys.*, 2004, **43**(1), 143–162.
17 N. Dencheva, Z. Denchev, M. J. Oliveira and S. Funari Sérgio, Microstructure Studies of In Situ Composites Based on Polyethylene/Polyamide 12 Blends, *Macromolecules*, 2010, **43**(10), 4715–4726.
18 H. Qiu, Y. Feng, Z. Hong, Y. Gao and J. Tan, Lightweight multi-layer graded pyramid folded structure based on tucked kirigami for green manufacturing, *Compos. Sci. Technol.*, 2024, **246**, 110383.
19 T. Zhang, Z. Dan, Z. Shen, J. Jiang, M. Guo, B. Chen, *et al.*, An alternating multilayer architecture boosts ultrahigh energy density and high discharge efficiency in polymer composites, *RSC Adv.*, 2020, **10**(10), 5886–5893.
20 F. Zhang, M. Guo, K. Xu, G. He, H. Wu and S. Guo, Multilayered damping composites with damping layer/constraining layer prepared by a novel method, *Compos. Sci. Technol.*, 2014, **101**, 167–172.
21 J. Du, S. R. Armstrong and E. Baer, Co-extruded multilayer shape memory materials: Comparing layered and blend architectures, *Polymer*, 2013, **54**(20), 5399–5407.
22 B. Chen, W. Gao, J. Shen and S. Guo, The multilayered distribution of intumescent flame retardants and its influence on the fire and mechanical properties of polypropylene, *Compos. Sci. Technol.*, 2014, **93**, 54–60.
23 X. Wang, M. Q. Romero, X. Q. Zhang, R. Wang and D. Y. Wang, Intumescent multilayer hybrid coating for flame retardant cotton fabrics based on layer-by-layer assembly and sol–gel process, *RSC Adv.*, 2015, **5**(14), 10647–10655.
24 S. Fateh Ali and J. Fan, Elastic-viscoplastic constitutive model for capturing the mechanical response of polymer composite at various strain rates, *J. Mater. Sci. Technol.*, 2020, **57**, 12–17.
25 C. H. Huang, J. S. Wu, C. C. Huang and L. S. Lin, Adhesion, Permeability, and Mechanical Properties of Multilayered Blown Films Using Maleated Low-Density Polyethylene Blends as Adhesion-Promoting Layers, *Polym. J.*, 2003, **35**(12), 978–984.
26 C. H. Huang, J. S. Wu and C. C. Huang, Predicting the permeability and tensile behavior of high density polyethylene/tie/polyamide 6 three-layer films, *Polym. Int.*, 2004, **53**(12), 2099–2106.
27 C. Ge, K. Lei and R. Aldi, Barrier, mechanical, and thermal properties of the three-layered co-extruded blown polyethylene/ethylene–vinyl alcohol/low density polyethylene film

without tie layers, *J. Thermoplast. Compos. Mater.*, 2017, **30**(6), 794–807.
28 W. Fang, Y. H. Cheng, A. Pearson, M. Duncan, J. Runka, A. Hammami, *et al.*, Carbon fiber reinforced polyethylene composite adhesive at elevated temperatures, *Compos. Sci. Technol.*, 2023, **244**, 110269.
29 T. Tang, H. Li and B. Huang, Compatibilization and structure of poly(propylene)/nylon–12 blends, *Macromol. Chem. Phys.*, 1994, **195**(8), 2931–2945.
30 A. Traidia, B. Craster, J. Rondin and A. Al Tamimi, Reduction in the transport of sour gases and hydrocarbons to underlying PE-RT through thin films of PVDF, *J. Memb. Sci.*, 2024, **694**, 122416.
31 D. C. Joy, Control of charging in low-voltage SEM, *Scanning*, 1989, **11**(1), 1–4.
32 F. Kar, J. Fan and W. Yu, Comparison of different test methods for the measurement of fabric or garment moisture transfer properties, *Meas. Sci. Technol.*, 2007, **18**(7), 2033–2038.
33 A. Dargahi, M. Duncan, J. Runka, A. Hammami and H. E. Naguib, Supercritical CO2 permeation in polymeric films: Design, characterization, and modeling, *Mater. Des.*, 2023, **227**, 111715.
34 M. Giacinti Baschetti and M. Minelli, Test methods for the characterization of gas and vapor permeability in polymers for food packaging application: A review, *Polym. Test.*, 2020, **89**, 106606.
35 A. Dargahi, R. Schultz, J. Runka, H. Ashrafizadeh, B. Xu and H. E. Naguib, Nonlinear creep characteristics of extruded Poly (vinylidene fluoride-co-hexafluoropropylene) with high ß-phase content under extreme conditions: Design, characterization, and modeling, *Mater. Des.*, 2023, **232**, 112124.
36 V. S. Chevali, D. R. Dean and G. M. Janowski, Flexural creep behavior of discontinuous thermoplastic composites: Nonlinear viscoelastic modeling and time–temperature–stress superposition, *Composites, Part A*, 2009, **40**(6–7), 870–877.
37 A. L. Wickeler and H. E. Naguib, Novel origami-inspired metamaterials: Design, mechanical testing and finite element modelling, *Mater. Des.*, 2020, **186**, 108242.
38 A. L. Wickeler and H. E. Naguib, 3D printed geometrically tessellated sheets with origami-inspired patterns, *J. Cell. Plast.*, 2022, **58**(2), 377–395.
39 A. Gnatowski and M. Sosnowski, Effect of PVP and Polybond Compatibilizers on Dynamic Properties of Polymer Blends Analyzed with DMTA, *Adv. Sci. Technol. Res. J.*, 2018, **12**(1), 36–40.
40 H. Sato, S. Sasao, K. Matsukawa, Y. Kita, T. Ikeda, H. Tashiro, *et al.*, Raman Mapping Study of Compatibilized and Uncompatibilized Polymer Blends of Nylon 12 and Polyethylene, *Appl. Spectrosc.*, 2002, **56**(8), 1038–1043.
41 T. Tang, H. Li and B. Huang, Compatibilization and structure of poly(propylene)/nylon-12 blends, *Macromol. Chem. Phys.*, 1994, **195**(8), 2931–2945.
42 H. Sato, S. Sasao, K. Matsukawa, Y. Kita, H. Yamaguchi, H. W. Siesler, *et al.*, Molecular Structure, Crystallinity, and Morphology of Uncompatibilized and Compatibilized Blends of Polyethylene/Nylon 12, *Macromol. Chem. Phys.*, 2003, **204**(10), 1351–1358.
43 W. Shao, L. Z. Liu, Y. Wang, Y. Wang, Y. Shi and L. Song, Investigation of Crystallization, Morphology, and Mechanical Properties of Polypropylene/Polypropylene-Polyethylene Block Copolymer Blends, *Polymers*, 2023, **15**(24), 4680.
44 N. S. Murthy, Hydrogen bonding, mobility, and structural transitions in aliphatic polyamides, *J. Polym. Sci., Part B: Polym. Phys.*, 2006, **44**(13), 1763–1782.
45 H. Sato, S. Sasao, K. Matsukawa, Y. Kita, H. Yamaguchi, H. W. Siesler, *et al.*, Molecular Structure, Crystallinity, and Morphology of Uncompatibilized and Compatibilized Blends of Polyethylene/Nylon 12, *Macromol. Chem. Phys.*, 2003, **204**(10), 1351–1358.
46 H. Sato, M. Isogai, S. Sasao, K. Matsukawa, Y. Kita, H. Yamaguchi, *et al.*, Raman and Wide–Angle X–Ray Diffraction Studies on Molecular Structure, Crystallinity, and Morphology of Uncompatibilized and Compatibilized Blends of High Molecular Weight Polyethylene/Nylon 12, *Macromol. Symp.*, 2005, **220**(1), 75–84.
47 L. M. Robeson, Polymer Blends in Membrane Transport Processes, *Ind. Eng. Chem. Res.*, 2010, **49**(23), 11859–11865.
48 S. E. Solovyov and A. Y. Goldman, Permeability of multilayer structures, *e-Polymers*, 2004, **4**(1), 023.
49 M. H. Klopffer and B. Flaconneche, Transport Properdines of Gases in Polymers: Bibliographic Review, *Oil Gas Sci. Technol.*, 2001, **56**(3), 223–244.
50 M. M. Feldstein, G. A. Shandryuk, S. A. Kuptsov and N. A. Platé, Coherence of thermal transitions in poly(N-vinyl pyrrolidone)–poly(ethylene glycol) compatible blends 1. Interrelations among the temperatures of melting, maximum cold crystallization rate and glass transition, *Polymer*, 2000, **41**(14), 5327–5338.
51 M. F. Ashby, Designing Hybrid Materials, in *Materials Selection in Mechanical Design*, Elsevier, 2011, pp. 299–340.
52 L. Grassia and A. D'Amore, Constitutive law describing the phenomenology of subyield mechanically stimulated glasses, *Phys. Rev. E: Stat., Nonlinear, Soft Matter Phys.*, 2006, **74**(2), 021504.
53 L. Grassia and A. D'Amore, On the interplay between viscoelasticity and structural relaxation in glassy amorphous polymers, *J. Polym. Sci., Part B: Polym. Phys.*, 2009, **47**(7), 724–739.
54 A. Graziano, S. Jaffer and M. Sain, Review on modification strategies of polyethylene/polypropylene immiscible thermoplastic polymer blends for enhancing their mechanical behavior, *J. Elastomers Plastics*, 2019, **51**(4), 291–336.
55 Z. Wu, C. Zhang, Y. Zhu, Z. Lu, H. Liu, B. Xu, *et al.*, Visualization of Macrophase Separation and Transformation in Immiscible Polymer Blends, *CCS Chem.*, 2023, **5**(3), 718–728.
56 G. Belingardi and R. Vadori, Low velocity impact tests of laminate glass-fiber-epoxy matrix composite material plates, *Int. J. Impact Eng.*, 2002, **27**(2), 213–229.